nature materials

Article

https://doi.org/10.1038/s41563-024-02048-y

Colloidal quantum dots enable tunable liquid-state lasers

Received: 15 January 2024

Accepted: 11 October 2024

Published online: 22 November 2024

Check for updates

Donghyo Hahm[1], Valerio Pinchetti[1], Clément Livache[1], Namyoung Ahn[1], Jungchul Noh[1], Xueyang Li[2], Jun Du[1,2], Kaifeng Wu[1,2] & Victor I. Klimov[1]

Present-day liquid-state lasers are based on organic dyes. Here we demonstrate an alternative class of liquid lasers that use solutions of colloidal quantum dots (QDs). Previous efforts to realize such devices have been hampered by the fast non-radiative Auger recombination of multicarrier states required for optical gain. Here we overcome this challenge by using type-(I + II) QDs, which feature a trion-like optical gain state with strongly suppressed Auger recombination. When combined with a Littrow optical cavity, static (non-circulated) solutions of these QDs exhibit stable lasing tunable from 634 nm to 575 nm. These results indicate the feasibility of technologically viable dye-like QD lasers that exhibit broad spectral tunability and, importantly, provide stable operation without the need for a circulation system—a standard attribute of traditional dye lasers. The latter opens the door to less complex and more compact devices that can be readily integrated with various optical and electro-optical systems. An additional advantage of these lasers is the wide range of potentially available wavelengths that can be selected by controlling the composition, size and structure of the QDs.

Chemically prepared semiconductor nanocrystals, or colloidal quantum dots (QDs), have been actively investigated as optical gain media for solution-processable lasers[1–3]. A majority of the reported studies have focused on solid-state systems such as close-packed QD films[4–9]. However, there is also a considerable interest in QD-enabled liquid-state lasers, analogous to existing dye lasers. Although dye lasers are less common than solid-state devices, they remain useful in research and diagnostics[10–13]. They are also uniquely suited for application in emerging areas such as optofluidics[14,15].

Factors limiting the performance of dye lasers include interference from non-emissive triplet states and material degradation under high pump intensities. These problems have been typically circumvented using free-floating jet streams. However, this complicates the device, increases its footprint and makes integration with other devices difficult. QDs are grown in liquid media and can be easily manipulated in solutions like large molecules[16]. This makes them well suited for the implementation of liquid lasers, which could potentially solve the problem of the limited stability of traditional dyes. However, initial attempts to realize lasing with solutions of ordinary QDs were not successful[1]. Although there are a few reports in the literature regarding amplified spontaneous emission[17] (ASE) and microcavity lasing[18–20] achieved with QD solutions, the initial demonstration of ASE[4] as well as the majority of the reported lasing studies have utilized solid-state QD films.

A primary complication in colloidal QD lasing is the fast non-radiative Auger recombination of multicarrier optical gain states, which competes with stimulated emission and hinders laser action[4,21]. Since the stimulated emission rate decreases with decreasing QD concentration, fast Auger decay becomes a particularly serious problem in the case of dilute gain media such as QD solutions. In fact, as established elsewhere[4], there is a critical QD concentration ($n_{QD,cr}$) below which laser action is not possible. It was further found that $n_{QD,cr}$ scales inversely with the optical gain relaxation time (τ_g), which is directly related to the lifetime of a multicarrier optical gain state.

Typically, optical gain in QDs is generated by two electron–hole (e–h) pair states or biexcitons. In standard (non-engineered) QDs, biexciton decay is dominated by non-radiative Auger recombination,

[1]Nanotechnology and Advanced Spectroscopy Team, C-PCS, Chemistry Division, Los Alamos National Laboratory, Los Alamos, NM, USA. [2]State Key Laboratory of Molecular Reaction Dynamics, Dalian Institute of Chemical Physics, Chinese Academy of Sciences, Dalian, China. e-mail: klimov@lanl.gov

https://doi.org/10.1038/s41563-024-02048-y

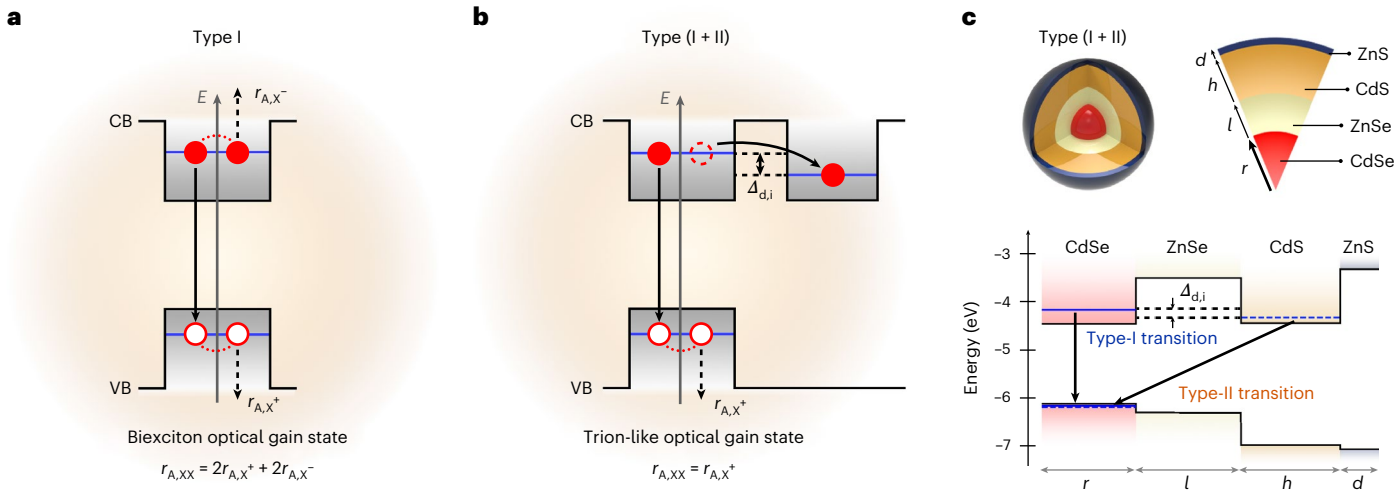

Fig. 1 | Ordinary versus hybrid biexcitons. a, In a conventional QD with colocalized electrons and holes (type-I QD), the optical gain is due to biexciton states. Their Auger recombination can be represented as a superposition of two negative-trion and two positive-trion pathways (rates r_{A,X^-} and r_{A,X^+} per pathway, respectively). CB and VB are the conduction and valence bands, respectively. **b**, In the proposed scheme, the optical gain is due to a hybrid biexciton consisting of a spatially direct and a spatially indirect exciton. Such biexcitons can be realized in the so-called type-(I + II) QDs. These structures contain an additional, indirect compartment in the conduction band, which captures an electron from the primary (direct) QD compartment, allowing the electron to reduce its energy. However, the energy difference ($\Delta_{d,i}$) driving electron transfer should be small enough to prevent the transfer of the second electron, which should remain in the primary compartment. This would lead to the creation of a hybrid direct/indirect biexciton. The Auger decay of such a biexciton occurs via a single positive-trion pathway. As a result, it is slower than that of a conventional biexciton. **c**, Practical implementation of type-(I + II) QDs. Top: schematic of the type-(I + II) CdSe/ZnSe/CdS/ZnS QD; *r*, *l*, *h* and *d* are the radius of the CdSe core, the thickness of the ZnSe barrier, the thickness of CdS interlayer and the thickness of the outer ZnS shell, respectively. Bottom: radial profiles of the electron and hole confinement potentials in the type-(I + II) QD. It features spatially direct (type I) and spatially indirect (type II) transitions (X_d and X_i excitons, respectively).

during which the e–h recombination energy is transferred to a third carrier[21]. Typical timescales of this process are extremely short (tens to hundreds of picoseconds depending on the QD size[21,22]), resulting in very short gain lifetimes and correspondingly high $n_{QD,cr}$ values (since $n_{QD,cr}$ scales as $1/\tau_g$), which are difficult to achieve with liquid QD samples due to solubility limits.

Here we resolve the problem of fast Auger decay using type-(I + II) QDs, which exhibit optical gain due to hybrid (direct/indirect) biexcitons with slow, charged-exciton-like relaxation dynamics. This reduces the critical concentration $n_{QD,cr}$ and allows us to realize stable, spectrally tunable liquid-state lasing using 'static' (non-circulated) solutions of the type-(I + II) QDs placed in a standard Littrow-type cavity.

Optical gain due to hybrid biexcitons

As mentioned earlier, most commonly, optical gain in a QD medium is due to neutral biexcitons (Fig. 1a) whose Auger lifetime ($\tau_{A,XX}$) determines the optical gain lifetime. On the basis of the 'universal' volume scaling[1,22], $\tau_{A,XX}$ ranges from ~4 ps to ~100 ps for typical colloidal QD diameters of ~2–6 nm, resulting in very short optical gain relaxation constants.

The gain lifetime can be increased by using charged excitons as optical gain species[23]. For example, due to the reduction in the number of recombination paths, the Auger lifetime of singly charged excitons (trions) can be four times (or more) longer than that of biexcitons[24]. Originally proposed in ref. 25, the charged-exciton gain mechanism has been used to practically demonstrate 'zero-threshold' optical gain[23,26] and 'sub-single-exciton' lasing[27]. The reported studies used QD films that were charged (doped) electrochemically[25,26], photochemically[23,27] or chemically[28].

Here we aim to realize the charged-exciton gain mechanism in QD solutions using specially designed particles in which biexcitons exhibit characteristics similar to those of charged excitons. The proposed QD design is shown in Fig. 1b. Along with the primary confinement volume (the 'direct' compartment), it contains an additional spatially separated ('indirect') electron compartment whose interaction with the primary volume is controlled by an interfacial potential barrier. The electron energy in the indirect compartment should be slightly lower than that in the primary QD volume, so that a single e–h pair is easily spatially separated, forming an indirect exciton. In the case of a biexciton, the energetic driving force should still be sufficient to facilitate the transfer of one electron to the indirect compartment. However, it should not be too large such that the Coulombic effects (attraction to the two holes in the direct compartment and repulsion from an electron in the indirect compartment) prevent the transfer of the second electron. As a result, the biexciton will be stabilized in a hybrid state consisting of a direct and indirect exciton.

An advantage of the hybrid biexciton for lasing applications is the increased Auger lifetime. For a standard biexciton, Auger decay can be described by a superposition of four recombination pathways, two associated with the positive trion and two with the negative trion (the rates per pathway are r_{A,X^+} and r_{A,X^-}, respectively)[24,29]. Therefore, the Auger decay rate of the biexciton can be expressed as $r_{A,XX} = 2r_{A,X^+} + 2r_{A,X^-}$ (Fig. 1a and Extended Data Fig. 1a). For the hybrid biexciton, the Auger dynamics are expected to be dominated by the carriers located in the direct compartment. Such carriers form a state similar to the positive trion, which decays via a single Auger pathway. Therefore, the decay rate is reduced to $r_{A,XX} = r_{A,X^+}$ (Fig. 1b and Extended Data Fig. 1b). On the basis of these considerations, we hypothesize that by implementing a hybrid biexciton gain scheme, we can increase the gain lifetime and therefore realize lasing with QD solutions.

Type-(I + II) QDs

To implement the hybrid biexciton scheme, we chose the core/multi-shell design (Fig. 1c, top). The proposed heterostructure comprises a CdSe core (direct compartment), a ZnSe shell (barrier layer), a CdS shell (indirect compartment) and a final ZnS layer added to enhance the QD stability. In the barrier layer, we grade the semiconductor composition using a $Cd_{1-x}Zn_xSe$ alloy for which *x* increases from 0 to 1 in the radial

https://doi.org/10.1038/s41563-024-02048-y

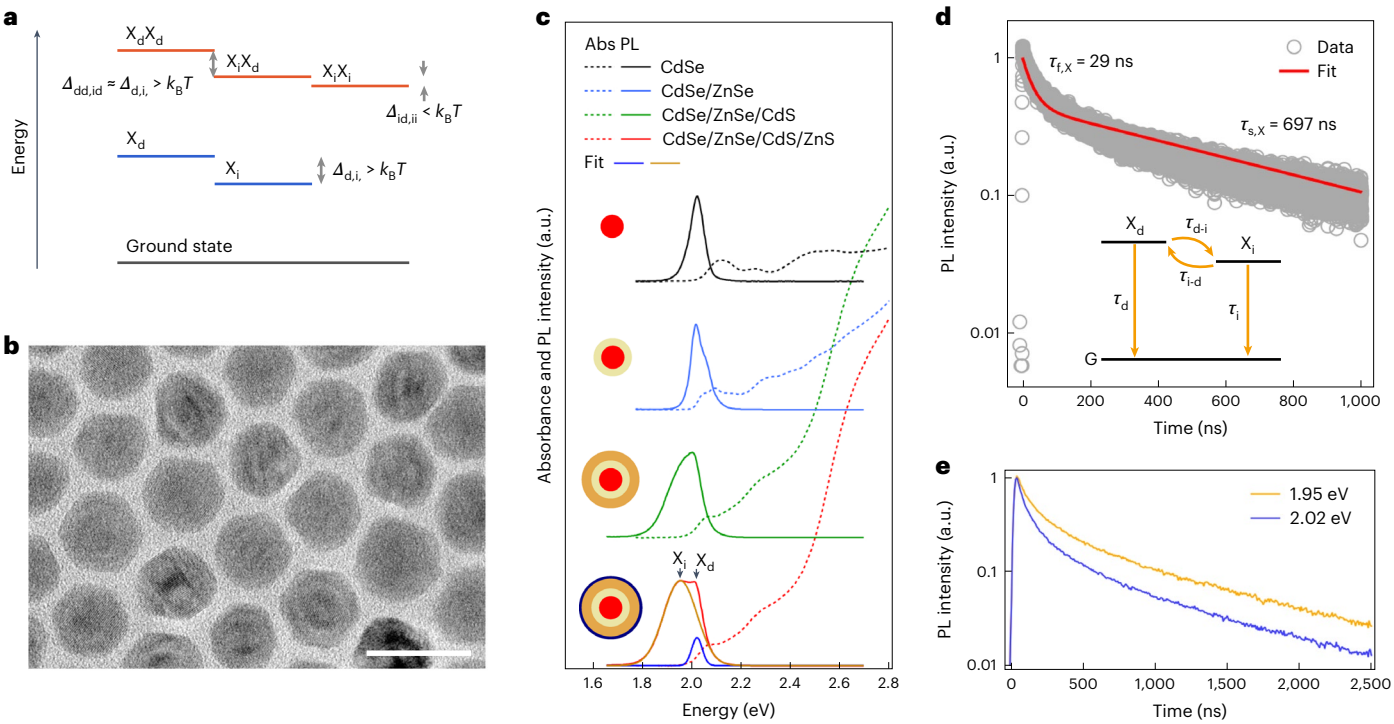

Fig. 2 | Structural and optical characteristics of type-(I + II) QDs. a, Energy levels of single exciton (blue) and biexciton (red) states in type-(I + II) QDs. To realize a stable hybrid X_iX_d biexciton, three conditions must be simultaneously met: $\Delta_{d,i} > k_BT$, $\Delta_{dd,id} > k_BT$ and $\Delta_{id,ii} < k_BT$. **b**, Transmission electron microscopy image of type-(I + II) QDs with $r = 2.6$ nm, $l = 1.7$ nm, $h = 2.2$ nm and $d = 0.3$ nm. Scale bar, 20 nm. **c**, Series of absorption and PL spectra (dashed and solid lines, respectively) recorded at different stages of the synthesis of type-(I + II) CdSe QDs shown in **b**. From top to bottom: CdSe cores, CdSe/ZnSe QDs, CdSe/ZnSe/CdS QDs and CdSe/ZnSe/CdS/ZnS QDs. The PL spectrum of the final type-(I + II) QDs (red) can be presented as a sum of two Gaussian profiles centred at 2.02 eV and 1.95 eV. These bands correspond to the direct (blue) and indirect (gold) transitions, respectively. All the PL spectra were acquired using continuous-wave (cw) 2.76 eV excitation. **d**, Measured spectrally integrated PL dynamics of type-(I + II) QDs (grey circles) together with modelling (red line) performed using a three-level scheme shown in the inset. The best agreement between the simulation and experiment was obtained for the following parameters: $\tau_d = 44$ ns, $\tau_i = 735$ ns, $\tau_{d\text{-}i} = 85$ ns and $\tau_{i\text{-}d} = 8.8$ µs. **e**, Spectrally resolved PL dynamics of type-(I + II) QDs measured at 1.95 eV (yellow) and 2.02 eV (blue). The faster component is more pronounced in the trace recorded at 2.02 eV, that is, near the centre of the direct exciton band.

direction. This helps to inhibit the Auger recombination for both neutral and charged multicarrier species[7] due to the suppression of intraband transition involving the energy-accepting carrier[30]. For simplicity, we refer to the barrier layer as the ZnSe shell or ZnSe barrier in this work.

The use of a wide-gap ZnSe shell allows us to create a confinement potential for both electron and hole (Fig. 1c, bottom), as required by the scheme shown in Fig. 1b. CdS used in the indirect compartment layer also has a bandgap that is wider than that of CdSe. At the same time, its conduction band edge is close to that of CdSe. Therefore, by changing the width of the CdS shell, we can fine-tune the energy of the electron in the indirect compartment compared with the energy in the core and consequently realize the desired regime in which charge transfer is favoured only for one electron of the biexciton state but not for two. When expressed quantitatively, these conditions can be expressed as $\Delta_{d,i} = E_d - E_i > k_BT$, $\Delta_{dd,id} = E_{dd} - E_{id} > k_BT$ and $\Delta_{id,ii} = E_{id} - E_{ii} < k_BT$ (Fig. 2a), hereafter referred to as hybrid biexciton conditions 1–3, respectively. Here E_d and E_i are the energies of direct (X_d) and indirect (X_i) excitons, respectively. E_{dd}, E_{ii} and E_{id} are the energies of all-direct (X_dX_d), all-indirect (X_iX_i) and hybrid direct/indirect (X_iX_d) biexcitons, respectively. T and k_B are the temperature and the Boltzmann constant, respectively.

To determine the range of QD parameters for which these three conditions can be satisfied, we applied the effective-mass approximation to calculate the energies of single excitons and biexcitons using the conduction- and valence-band confinement potentials shown in Fig. 1c and taking into account the carrier–carrier Coulomb interactions (Supplementary Note 1)[31]. The latter is an essential part of the simulation since the 'giant' exciton–exciton repulsion characteristic of an all-indirect biexciton[31,32] is required to raise the energy of the X_iX_i state above the energy of two non-interacting X_i excitons and thus simultaneously satisfy conditions 1 and 3, leading to stable hybrid biexcitons.

Extended Data Fig. 2 shows the region of energetic stability of the hybrid biexciton in the coordinates l (ZnSe barrier width) and h (CdS shell thickness), calculated for a fixed CdSe core radius ($r = 2.6$ nm) and a fixed ZnS layer thickness ($d = 0.3$ nm) at $T = 300$ K (room temperature). In the same diagram, we also show the region for which the lowest and first excited e–h (exciton) states are of well-defined indirect and direct characters, respectively, as indicated by the calculated values of the e–h overlap integral ($\theta_{eh} < 0.1$ and $\theta_{eh} > 0.9$, respectively). According to this simulation, the realization of hybrid direct/indirect biexcitons requires l of at least ~1.3 nm and h of at least ~1.8 nm. Typically, QDs are classified as type I if their band-edge transition is associated with a spatially direct exciton and as type II if the band-edge exciton is spatially indirect. Since the targeted heterostructures are expected to simultaneously support both direct and indirect excitons, we call them type-(I + II) QDs.

To realize type-(I + II) QDs with the desired hybrid biexciton characteristics, we synthesized CdSe/ZnSe/CdS/ZnS samples with $r = 2.6$ nm, $l = 1.7$ nm, $h = 2.2$ nm and $d = 0.3$ nm (Extended Data Fig. 2a (red circle); the Methods provides the synthesis details). The transmission electron microscopy images of the synthesized structures are shown in Fig. 2b (final CdSe/ZnSe/CdS/ZnS QDs) and Extended Data Fig. 3 (final and intermediate structures). The synthesized QDs exhibit excellent monodispersity (size standard deviation, <8%) and show

https://doi.org/10.1038/s41563-024-02048-y

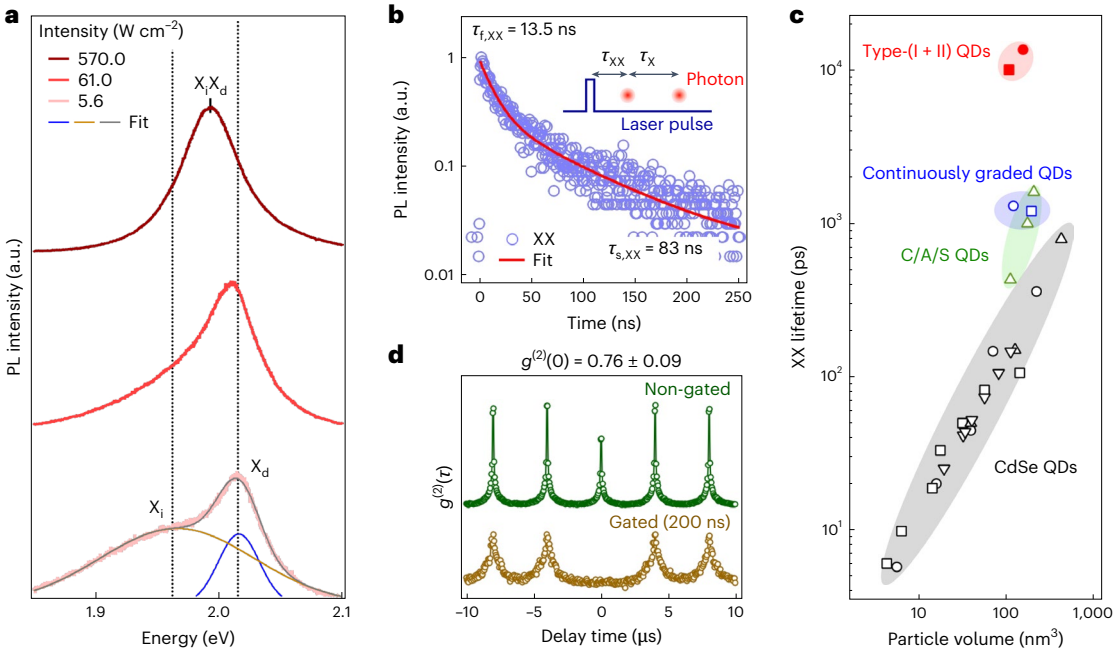

Fig. 3 | Biexcitons in type-(I + II) QDs. a, Pump-intensity-dependent PL spectra for a single type-(I + II) QD recorded using cw 2.54 eV excitation. The spectrum with the lowest pump intensity is decomposed into two bands corresponding to direct (X_d) and indirect (X_i) excitons. All the panels in this figure belong to the same type-(I + II) QD sample as that shown in Fig. 2. **b**, Single-dot measurements of biexciton PL decay (blue circles). These data were obtained using the Hanbury Brown-Twiss (HBT) experiment, which allows the identification of excitation cycles with two emitted photons and the derivation of the biexciton lifetime from the delay of the first photon relative to the pump pulse (inset). The red line represents a biexponential fit, which yields time constants of 13.5 ns and 83 ns for the fast ($\tau_{f,XX}$) and slow ($\tau_{s,XX}$) relaxation components, respectively. **c**, Biexciton lifetime as a function of effective QD volume for different QD types: plain CdSe core-only QDs[21,38–40] (black), core/alloy/shell (C/A/S) CdSe/$CdSe_{0.5}S_{0.5}$/CdS QDs[1] (green), CdSe/$Cd_xZn_{1-x}Se$/$ZnSe_{0.5}S_{0.5}$ cg-QDs[7,17] (blue) and type-(I + II) QDs from the present study (red) with CdSe core radii of 2.3 nm (square) and 2.6 nm (circle). The effective volumes were calculated from the size of the sphere that confines charge carriers with a probability of 99% (ref. 41). **d**, Single-dot measurements of the second-order intensity correlation ($g^{(2)}$) function without photon discrimination (top, green line) and with photon discrimination (bottom, gold line) performed by selecting ('gating') photons with a time delay of more than 200 ns time relative to the pump pulse. The non-gated $g^{(2)}(0)$ averaged over 26 QDs, is 0.76 (derived from the measurements without photon discrimination). This value gives the ratio of the quantum yields of the biexciton and single-exciton emission. The fact that the gated $g^{(2)}(0)$ is close to zero confirms that the measurements were performed on a single QD, and not on a cluster containing several QDs.

the expected Cd, Zn, S and Se compositional profiles measured by energy-dispersive X-ray spectroscopy (Extended Data Fig. 3).

In Fig. 2c, we show a series of absorption and photoluminescence (PL) spectra of the structures that occur at different growth stages of the type-(I + II) QDs. The PL spectrum evolves from a spectrally symmetric single-band emission due to e–h radiative recombination in the CdSe cores (Fig. 2c, black solid line) to a double-hump structure in the case of CdSe/ZnSe/CdS/ZnS QDs (Fig. 2c, red solid line). The emergence of the lower-energy PL feature indicates the formation of a lower-energy indirect exciton (X_i) consisting of an electron in the CdS shell and a hole in the CdSe core. On the basis of the dual-band deconvolution of the PL spectrum (Supplementary Fig. 1), the energies of the direct and indirect excitons are 2.02 eV and 1.95 eV, respectively, which satisfy the required condition $E_d - E_i = 70$ meV $> k_BT$. The measured values are also in reasonable agreement with those obtained from our simulations ($E_i = 1.99$ eV and $E_d = 2.04$ eV; Supplementary Note 1 and Supplementary Fig. 2). The dual-exciton character of the emission of the final hetero-QDs is also evident in the PL excitation measurements (Supplementary Fig. 3) and single-dot PL spectra (Supplementary Fig. 4a).

In addition to its manifestation in the PL and PL excitation spectra, the two-state emission mechanism is evident in the PL dynamics. In particular, PL exhibits double-exponential relaxation in both ensemble (Fig. 2d) and single-dot (Supplementary Fig. 4b) measurements, which reveal distinct fast ($\tau_{f,X} = 29$ ns) and slow ($\tau_{s,X} = 697$ ns) components. As expected, the fast signal is more pronounced in the spectral range of the higher-energy peak associated with the X_d state, whereas the slowly relaxing component is enhanced in the range of the X_i exciton (Fig. 2e).

The measured biexponential PL dynamics and the relative intensities of the X_d and X_i PL features can be quantitatively described using a model of two coupled electron states (related to the direct and indirect compartments of the QD) emitting via optical transitions involving a common hole state in the direct compartment (Fig. 2d (inset) and Supplementary Note 2). On the basis of the simulation of the measured PL dynamics (Fig. 2d), the radiative X_d and X_i lifetimes are $\tau_d = 44$ ns and $\tau_i = 735$ ns, and the $X_d \rightarrow X_i$ and $X_i \rightarrow X_d$ population transfer time constants are $\tau_{d\text{-}i} = 85$ ns and $\tau_{i\text{-}d} = 8.8$ μs. The fact that $\tau_{d\text{-}i}$ is longer than τ_d is important to explain the discernible PL signal from the X_d state, which is energetically higher than the X_i state.

The above analysis confirms that the prepared QDs indeed simultaneously support direct and indirect excitons, as expected based on their dimensions, which correspond to the type-(I + II) region shown in Extended Data Fig. 2 (red circle). Importantly, when we synthesized QD samples whose dimensions were outside the type-(I + II) region, their measured characteristics were consistent with those of traditional type-I and quasi-type-II QDs[31,33] (Extended Data Fig. 2, blue square and black triangle, respectively), which is again in agreement with our calculations.

Biexcitons in type-(I + II) QDs

On the basis of the modelling of biexciton states (Supplementary Note 1), the X_iX_i and X_iX_d biexcitons in the synthesized type-(I + II) QDs have comparable energies (4.020 eV and 4.024 eV, respectively), which are considerably lower than the energy of the X_dX_d biexciton ($E_{dd} = 4.07$ eV). Importantly, all three energies satisfy the conditions

$\Delta_{dd,id} > k_B T$ and $\Delta_{id,ii} < k_B T$, for which the biexciton emission should be dominated by the hybrid direct/indirect state.

Since the X_iX_d biexciton is anticipated to emit mainly via the direct transition, its radiative decay should produce an X_i exciton. The same final state is generated by the radiative recombination of the X_iX_i biexciton. Therefore, the expected biexciton emission energies are $h\nu_{ii} = E_{ii} - E_i = 2.03$ eV and $h\nu_{id} = E_{id} - E_i = 2.04$ eV. Both values are close to the energy of the X_d state (2.04 eV), which is why the double-hump PL spectrum should be gradually replaced with a narrower single-band spectrum (near the X_d PL feature) as the photoexcited system evolves from the exciton to the biexciton state with increasing excitation intensity.

This expected trend is well expressed in the measured single-dot PL spectra. At low, sub-single-exciton pump levels, the PL line shape indicates the presence of two distinct transitions due to direct and indirect excitons (Fig. 3a). As the pump level increases, the relative contribution of the lower-energy X_i feature gradually decreases and the spectra become dominated by a single band located slightly below the X_d energy. At the same time, we detect the expected narrowing of the emission profile from 107 meV to 57 meV. Similar trends are systematically observed for other measured QDs (Extended Data Fig. 4). Due to highly stable (virtually, 'non-blinking') single-dot emission (Extended Data Fig. 5), these trends are consistently reproduced in repeated measurements of the same QD.

Although the two biexcitonic components are not easily distinguished in the PL spectra, they appear as distinct components in the PL time transients. In particular, the single-dot biexciton dynamics (Fig. 3b) exhibit a two-component decay with time constants of 13.5 ns ($\tau_{f,XX}$) and 83 ns ($\tau_{s,XX}$), which we attribute to the X_iX_d and X_iX_i states, respectively. The fast biexciton PL component is contributed by the recombination of the X_iX_d state (radiative and Auger) and its population exchange with the X_iX_i state. From this, the X_iX_d recombination time is 13.5 ns or longer, indicating a strong suppression of Auger recombination. In fact, this time constant is an order of magnitude longer than the biexciton lifetimes previously reported for plain and engineered CdSe-based QDs including continuously graded CdSe/$Cd_{1-x}Zn_xSe$ QDs (cg-QDs) specifically designed to impede Auger decay[7,34] (Fig. 3c). The strong suppression of Auger decay in type-(I + II) QDs is also indicated by the high biexciton emission efficiency (q_{XX}). In particular, q_{XX}, determined either from the PL dynamics (Supplementary Note 3) or from single-dot two-photon correlation measurements (Methods), is consistently between ~60% and ~76%. (Fig. 3d, Supplementary Fig. 5 and Supplementary Table 1).

Optical gain in type-(I + II) QDs

Due to the hindered Auger decay, type-(I + II) QDs exhibit excellent optical gain properties. Femtosecond transient absorption (TA) measurements (Methods) show that the optical gain bandwidth reaches ~300 meV at $\langle N \rangle = 34.3$ (Fig. 4a; $\langle N \rangle$ is the average number of e–h pairs generated per QD per pump pulse), which is similar to the optical gain bandwidth of organic laser dyes[35] (Supplementary Table 2). At the same pump level, the gain lifetime is ~3.0 ns (Fig. 4b). This is larger than τ_g previously observed for quantum-confined CdSe-based nanocrystals, including cg-QD samples (Supplementary Table 1)[1,17] and comparable to the τ_g values of very large CdS nanocrystals for which Auger decay is absent due to the bulk-like character of the electronic states[8]. The type-(I + II) QDs also exhibit a large peak material gain reaching 1,110 cm^{-1}, as indicated by the TA measurements (Fig. 4a and Supplementary Table 1).

Liquid-state lasing with type-(I + II) QDs

The increased optical gain lifetime in type-(I + II) QDs results in a decrease in the critical concentration required for lasing. In particular, using $\tau_g = 3.0$ ns, we estimate $n_{QD,cr}$ to be ~6×10^{15} cm^{-3} or ~10 μmol l^{-1} (Supplementary Note 4)[1,36]. Such concentrations are readily available using standard toluene solutions of type-(I + II) QDs.

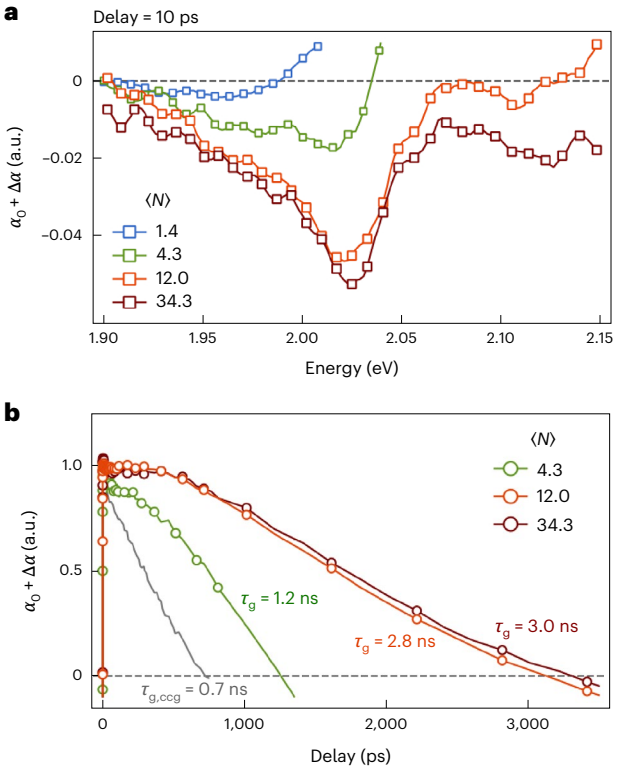

Fig. 4 | Optical gain in type-(I + II) QDs. a, TA spectra of type-(I + II) QDs (same sample as that in Figs. 2 and 3) presented as the excited-state absorption coefficient (α) for a pump–probe delay of 10 ps and for excitation levels $\langle N \rangle = 1.4$–34.3 (190 fs, 2.4 eV pump pulses). $\alpha = \alpha_0 + \Delta\alpha$, where α_0 is the ground-state absorption coefficient (unexcited sample) and $\Delta\alpha$ is the pump-induced absorption change. The optical gain appears as $\alpha < 0$. **b**, TA dynamics yield optical gain lifetimes (τ_g) up to 3.0 ns. The gain dynamics of compact cg-QDs ($\tau_{g,ccg}$) from another work[17] are included for comparison (grey line).

To realize wavelength-tunable liquid-state QD lasing, we use a Littrow-type resonator[37] that includes a highly reflective planar mirror and a reflection grating whose angle controls the cavity resonance (Fig. 5a and Methods). A QD solution with a concentration of 14 μmol l^{-1} (slightly higher than the estimated $n_{QD,cr}$) loaded into a standard 1-mm-thick quartz cuvette serves as the gain medium. The QDs are excited using 2.33 eV, 5 ns second-harmonic pulses from a neodymium-doped yttrium aluminium garnet (Nd:YAG) laser.

In Fig. 5b, we show the measurements of the output-beam intensity as a function of the per-pulse pump fluence (J_p) for the situation in which the cavity is tuned to 1.984 eV. When J_p reaches 44 mJ cm^{-2}, an intense beam emerges from the cavity. It is highly directional and is detected as a bright spot with a radius of 1.8 mm at a distance of 2.5 m from the cavity (Fig. 5c). The measurements of beam profile yield a divergence half-angle of $\theta = 0.66$ mrad (or only 0.038°) and a beam waist radius of $w_0 = 0.28$ mm (Fig. 5d).

As shown in Fig. 5b (inset), the emitted light is characterized by a narrow linewidth of 2 meV (full-width at half-maximum Γ). This value is in agreement with the measured coherence time (τ_c) of 0.7 ps (Extended Data Fig. 6), which corresponds to $\Gamma = 1.9$ meV (calculated using $\Gamma = h/(\pi\tau_c)$; h is Planck's constant). The linewidth can be further narrowed to 0.38 meV or 1.2 Å (Fig. 5e, inset) by including a beam expander into the cavity, which improves its spectral selectivity by increasing the size of the illuminated region of the grating.

Polarization measurements (Extended Data Fig. 7) show that the emitted light is almost perfectly linearly polarized (~95% degree of polarization) in the direction perpendicular to the grooves of the Littrow grating. This is a result of the strong dependence of the grating

https://doi.org/10.1038/s41563-024-02048-y

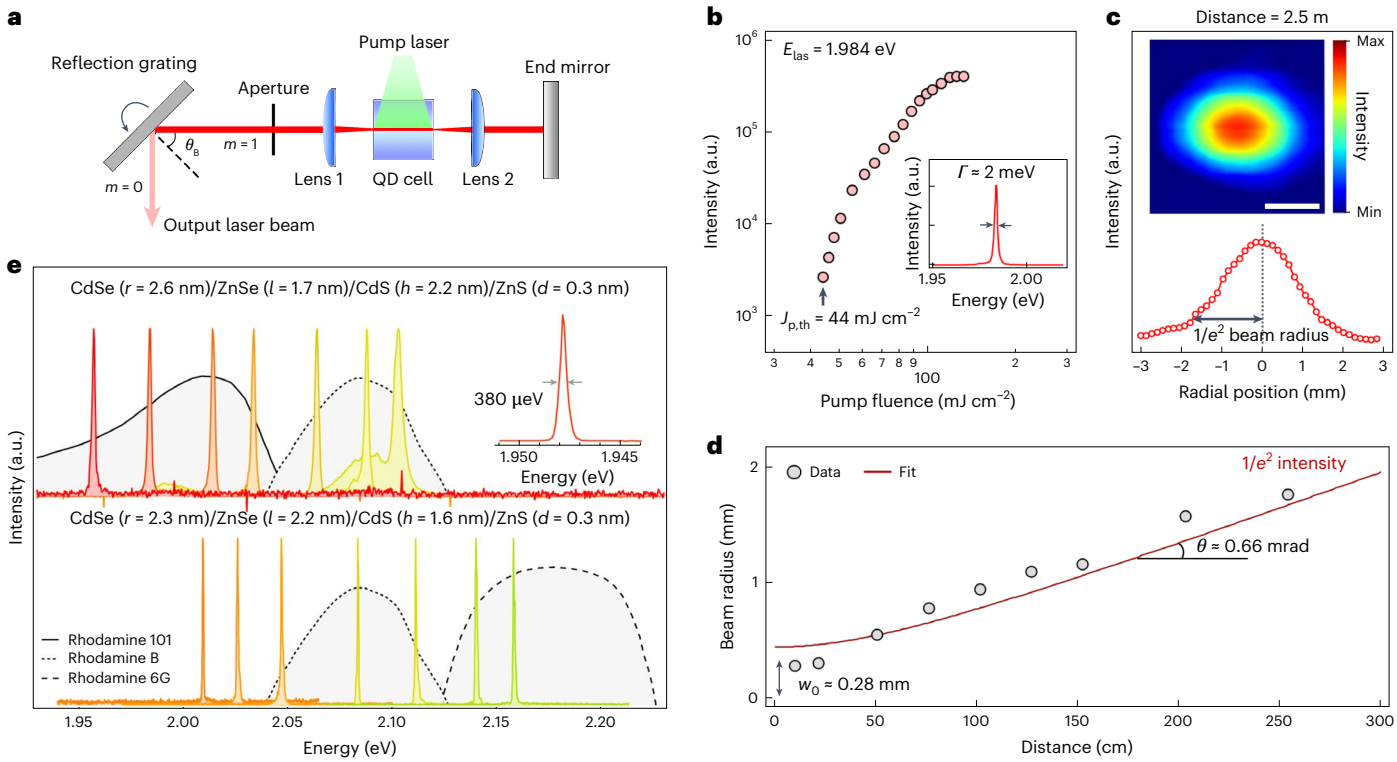

Fig. 5 | Liquid-state lasing using type-(I + II) QDs. a, Schematic of a liquid laser with a solution of type-(I + II) QDs as the optical gain medium, incorporated into a wavelength-tunable Littrow resonator consisting of a planar mirror and a reflection grating. Intracavity elements (two lenses and an aperture) help to collimate the beam and improve its cross-section profile. **b**, Output-beam intensity as a function of pump fluence for type-(I + II) QDs with r = 2.6 nm (same QDs as those shown in Figs. 2 to 4). The QD sample (concentration, 14 μmol l^{-1}) is excited by 2.33 eV, 5 ns, 10 Hz second-harmonic pulses of a Nd:YAG laser. The sharp onset of highly directional emission from the cavity at 1.984 eV occurs at j_p = 44 mJ cm^{-2}, which corresponds to the lasing threshold. Inset: the emitted light is characterized by a narrow linewidth (Γ) of 2 meV. **c**, Radial intensity profile (bottom) obtained from the two-dimensional intensity distribution (top; scale bar, 1 mm) of the output beam measured at a distance of 2.5 m from the cavity. The beam radius (at the intensity level 1/e^2) is 1.8 mm. **d**, Beam radius as a function of distance from the cavity (circles), fitted to a hyperbola (line). On the basis of these measurements, the divergence half-angle (θ) is 0.66 mrad (or 0.038°) and the beam waist radius (w_0) is 0.28 mm. **e**, Using QDs with CdSe core radii of 2.6 nm and 2.3 nm, the lasing line can be tuned from 1.96 eV to 2.10 eV (633 to 590 nm) and from 2.01 eV to 2.16 eV (617 to 574 nm), respectively. Inset: the lasing spectrum of a device containing a beam expander in the cavity indicates a linewidth of 380 μeV (or 1.2 Å). For comparison, the lasing efficiency spectra of traditional rhodamine dyes (6G, B and 101) are shown with grey shading (based on data from Radiant Dyes Laser & Accessories).

reflectivity on the polarization of the incident light (~80% and ~15% for *p*- and *s*-polarized light, respectively).

The narrow linewidth of the emitted light, low beam divergence and nearly perfect linear polarization clearly indicate the implementation of the lasing regime. We can exclude that the observed effect is due to ASE as the ASE signal is observed as a broader, low-amplitude spectrally distinct band, the threshold of which exceeds the lasing threshold (Extended Data Fig. 8).

To test for the reproducibility of the laser action, we synthesized and studied three additional batches of type-(I + II) QDs with parameters nominally identical to those of the QDs shown in Fig. 5b–d. All the additional samples exhibited lasing in the liquid state. Tests of gradually diluted samples showed that stable lasing can be realized at QD concentrations as low as ~8 μmol l^{-1}, which is close to the calculated $n_{QD,cr}$ value (~10 μmol l^{-1}).

By changing the grating blaze angle, we can tune the lasing line from 1.96 eV to 2.10 eV (633 nm to 590 nm, respectively; Fig. 5e, coloured lines). The tunability range achieved with a single QD sample simultaneously covers the lasing windows of two popular laser dyes, rhodamine B and rhodamine 101 (Fig. 5e, black dotted and solid lines, respectively).

We can further extend the range of the covered spectral energies by exploiting the bandgap tunability of QDs by controlling the particle size. In particular, by using type-(I + II) QDs with a smaller CdSe core (r = 2.3 nm) and a correspondingly larger bandgap (2.08 eV; Extended Data Fig. 9 shows the details of the sample structure and spectroscopic characteristics), we could realize lasing at higher spectral energies (from 2.01 eV to 2.16 eV; Fig. 5e, bottom panel), which reach the lasing range of rhodamine 6G. Thus, in addition to the broadband spectral tunability realizable with a single QD sample, the QD approach allows for the easy shifting of the entire lasing window to a desired wavelength range through the easy manipulation of QD size and/or composition.

Another useful characteristic of QDs is their high operational stability, achieved without sample agitation (for example, by stirring or flowing). This is an important advantage compared with laser dyes, which require high-speed circulation for stable operation. For example, although rhodamine 6G exhibits a lower lasing threshold when used instead of QDs in our Littrow cavity configuration (Supplementary Table 2), its output intensity degrades rapidly (in less than an hour) even when the device is operated just slightly above the lasing threshold (Extended Data Fig. 10). In contrast, 'static' solutions of type-(I + II) QDs show no signs of degradation over 5 h of continuous operation (Extended Data Fig. 10). At the same time, they exhibit a broader optical gain profile and a wider range of lasing tunability when compared side by side with rhodamine 6G (Supplementary Table 2).

In summary, our results demonstrate the considerable potential of type-(I + II) QDs as a direct alternative to traditional laser dyes. Importantly, QD lasers do not require the circulation of the gain medium

for stable operation. This should simplify the laser design compared with existing dye-based systems and reduce the device footprint. The elimination of circulation also removes safety concerns due to, for example, accidental splashing, expanding the scope of applications to areas currently inaccessible to dye lasers due to safety regulations. The additional advantages of QD solutions as liquid optical gain media stem from the unrivalled flexibility of their chemical properties and optical characteristics. All these features should prompt renewed interest in liquid lasers in the context of both traditional applications (for example, compact wavelength converters) and emerging technologies including optofluidics, lab-on-a-chip diagnostics and high-contrast sensing and imaging.

Online content

Any methods, additional references, Nature Portfolio reporting summaries, source data, extended data, supplementary information, acknowledgements, peer review information; details of author contributions and competing interests; and statements of data and code availability are available at https://doi.org/10.1038/s41563-024-02048-y.

References

1. Park, Y.-S., Roh, J., Diroll, B. T., Schaller, R. D. & Klimov, V. I. Colloidal quantum dot lasers. *Nat. Rev. Mater.* **6**, 382–401 (2021).
2. Geiregat, P., Van Thourhout, D. & Hens, Z. A bright future for colloidal quantum dot lasers. *NPG Asia Mater.* **11**, 41 (2019).
3. Ahn, N., Livache, C., Pinchetti, V. & Klimov, V. I. Colloidal semiconductor nanocrystal lasers and laser diodes. *Chem. Rev.* **123**, 8251–8296 (2023).
4. Klimov, V. I. et al. Optical gain and stimulated emission in nanocrystal quantum dots. *Science* **290**, 314–317 (2000).
5. García-Santamaría, F. et al. Suppressed Auger recombination in 'giant' nanocrystals boosts optical gain performance. *Nano Lett.* **9**, 3482–3488 (2009).
6. Yakunin, S. et al. Low-threshold amplified spontaneous emission and lasing from colloidal nanocrystals of caesium lead halide perovskites. *Nat. Commun.* **6**, 8056 (2015).
7. Lim, J., Park, Y.-S. & Klimov, V. I. Optical gain in colloidal quantum dots achieved by direct-current charge injection. *Nat. Mater.* **17**, 42–49 (2018).
8. Tanghe, I. et al. Optical gain and lasing from bulk cadmium sulfide nanocrystals through bandgap renormalization. *Nat. Nanotechnol.* **18**, 1423–1429 (2023).
9. Dang, C. et al. Red, green and blue lasing enabled by single-exciton gain in colloidal quantum dot films. *Nat. Nanotechnol.* **7**, 335–339 (2012).
10. Nikaido, M., Mizuse, K. & Ohshima, Y. Torsional wave-packet dynamics in 2-fluorobiphenyl investigated by state-selective ionization-detected impulsive stimulated Rraman spectroscopy. *J. Phys. Chem. A* **127**, 4964–4978 (2023).
11. Suryanarayana, M. Isotope separation of ^{176}Lu a precursor to ^{177}Lu medical isotope using broadband lasers. *Sci. Rep.* **11**, 6118 (2021).
12. Tang, R. et al. Candidate for laser cooling of a negative ion: high-resolution photoelectron imaging of Th^-. *Phys. Rev. Lett.* **123**, 203002 (2019).
13. Henderson, B. W. *Photodynamic Therapy: Basic Principles and Clinical Applications*. Vol. 1 (CRC Press, 1992).
14. Li, Z. & Psaltis, D. Optofluidic dye lasers. *Microfluid. Nanofluid.* **4**, 145–158 (2008).
15. Schmidt, H. & Hawkins, A. R. The photonic integration of non-solid media using optofluidics. *Nat. Photon.* **5**, 598–604 (2011).
16. Murray, C. B., Norris, D. J. & Bawendi, M. G. Synthesis and characterization of nearly monodisperse CdE (E=S, Se, Te) semiconductor nanocrystallites. *J. Am. Chem. Soc.* **115**, 8706–8715 (1993).
17. Li, X. et al. Two-color amplified spontaneous emission from Auger-suppressed quantum dots in liquids. *Adv. Mater.* **36**, 2308979 (2023).
18. Kazes, M., Lewis, D. Y., Evenstein, Y., Mokari, T. & Banin, U. Lasing from semiconductor quantum rods in a cylindrical microcavity. *Adv. Mater.* **14**, 317–321 (2002).
19. Wang, Y. et al. Blue liquid lasers from solution of CdZnS/ZnS ternary alloy quantum dots with quasi-continuous pumping. *Adv. Mater.* **27**, 169–175 (2015).
20. Maskoun, J. et al. Optical microfluidic waveguides and solution lasers of colloidal semiconductor quantum wells. *Adv. Mater.* **33**, 2007131 (2021).
21. Klimov, V. I., Mikhailovsky, A. A., McBranch, D. W., Leatherdale, C. A. & Bawendi, M. G. Quantization of multiparticle Auger rates in semiconductor quantum dots. *Science* **287**, 1011–1013 (2000).
22. Robel, I., Gresback, R., Kortshagen, U., Schaller, R. D. & Klimov, V. I. Universal size-dependent trend in Auger recombination in direct-gap and indirect-gap semiconductor nanocrystals. *Phys. Rev. Lett.* **102**, 177404 (2009).
23. Wu, K., Park, Y.-S., Lim, J. & Klimov, V. I. Towards zero-threshold optical gain using charged semiconductor quantum dots. *Nat. Nanotechnol.* **12**, 1140–1147 (2017).
24. Wu, K., Lim, J. & Klimov, V. I. Superposition principle in Auger recombination of charged and neutral multicarrier states in semiconductor quantum dots. *ACS Nano* **11**, 8437–8447 (2017).
25. Wang, C., Wehrenberg, B. L., Woo, C. Y. & Guyot-Sionnest, P. Light emission and amplification in charged CdSe quantum dots. *J. Phys. Chem. B* **108**, 9027–9031 (2004).
26. Geuchies, J. J. et al. Quantitative electrochemical control over optical gain in quantum-dot solids. *ACS Nano* **15**, 377–386 (2021).
27. Kozlov, O. V. et al. Sub–single-exciton lasing using charged quantum dots coupled to a distributed feedback cavity. *Science* **365**, 672–675 (2019).
28. Whitworth, G. L., Dalmases, M., Taghipour, N. & Konstantatos, G. Solution-processed PbS quantum dot infrared laser with room-temperature tunable emission in the optical telecommunications window. *Nat. Photon.* **15**, 738–742 (2021).
29. Park, Y.-S., Bae, W. K., Pietryga, J. M. & Klimov, V. I. Auger recombination of biexcitons and negative and positive trions in individual quantum dots. *ACS Nano* **8**, 7288–7296 (2014).
30. Cragg, G. E. & Efros, A. L. Suppression of Auger processes in confined structures. *Nano Lett.* **10**, 313–317 (2010).
31. Piryatinski, A., Ivanov, S. A., Tretiak, S. & Klimov, V. I. Effect of quantum and dielectric confinement on the exciton–exciton interaction energy in type II core/shell semiconductor nanocrystals. *Nano Lett.* **7**, 108–115 (2007).
32. Klimov, V. I. et al. Single-exciton optical gain in semiconductor nanocrystals. *Nature* **447**, 441–446 (2007).
33. Brovelli, S. et al. Nano-engineered electron–hole exchange interaction controls exciton dynamics in core–shell semiconductor nanocrystals. *Nat. Commun.* **2**, 280 (2011).
34. Ahn, N. et al. Electrically driven amplified spontaneous emission from colloidal quantum dots. *Nature* **617**, 79–85 (2023).
35. Schäfer, F. P. *Dye Lasers* Vol. 1 (Springer Science & Business Media, 2013).
36. Park, Y.-S., Bae, W. K., Baker, T., Lim, J. & Klimov, V. I. Effect of Auger recombination on lasing in heterostructured quantum dots with engineered core/shell interfaces. *Nano Lett.* **15**, 7319–7328 (2015).
37. Littman, M. G. & Metcalf, H. J. Spectrally narrow pulsed dye laser without beam expander. *Appl. Opt.* **17**, 2224–2227 (1978).
38. Pandey, A. & Guyot-Sionnest, P. Multicarrier recombination in colloidal quantum dots. *J. Chem. Phys.* **127**, 111104 (2007).
39. Fisher, B., Caruge, J.-M., Chan, Y.-T., Halpert, J. & Bawendi, M. G. Multiexciton fluorescence from semiconductor nanocrystals. *Chem. Phys.* **318**, 71–81 (2005).

40. Achermann, M., Hollingsworth, J. A. & Klimov, V. I. Multiexcitons confined within a subexcitonic volume: spectroscopic and dynamical signatures of neutral and charged biexcitons in ultrasmall semiconductor nanocrystals. *Phys. Rev. B* **68**, 245302 (2003).
41. Park, Y.-S., Lim, J., Makarov, N. S. & Klimov, V. I. Effect of interfacial alloying versus 'volume scaling' on Auger recombination in compositionally graded semiconductor quantum dots. *Nano Lett.* **17**, 5607–5613 (2017).

Methods

Chemicals

Cadmium oxide (99.5%, trace metals basis), zinc acetate (99.99%, trace metals basis), oleic acid (OA, 90%, technical grade), 1-octadecene (ODE, 90%, technical grade), 1-octanethiol (≥98.5%), selenium (Se, ≥99.99%, trace metals basis) and sulfur (S, ≥99.0%) were purchased from Sigma-Aldrich. Tri-*n*-octylphosphine (TOP, 97%) was purchased from Strem Chemicals. All chemicals were used as received.

Precursor preparation

All the chemical procedures were conducted in an inert atmosphere using the Schlenk line technique. Before the QD synthesis, stock solutions of 0.5 M zinc oleate, 0.5 M cadmium oleate ($Cd(OA)_2$), 2 M TOPSe and 2 M TOPS were prepared. For the $Zn(OA)_2$ stock solution, a mixture of 100 mmol zinc acetate and a stoichiometric amount of OA were loaded into a flask and degassed under a vacuum at 140 °C for 2 h to achieve a clear solution. The flask was then purged with nitrogen, and the precursor concentrations were adjusted to 0.5 M using ODE. These precursor solutions were stored under an inert atmosphere at 100 °C for future use. To prepare the 0.5 M $Cd(OA)_2$ precursor solution, a combination of 20 mmol cadmium oxide, 20 ml OA and 20 ml ODE was degassed in a vacuum at 110 °C. The mixture was slowly heated to 300 °C to obtain a transparent solution. The reaction flask was subsequently cooled to 110 °C and vacuum-degassed again to eliminate any residual water. Stock solutions of 2 M TOPSe and TOPS were prepared by dissolving 100 mmol of Se and S in 50 ml of TOP at an elevated temperature. These stock solutions were then stored in a glove box for future use.

Synthesis of type-(I + II) QDs

Below, we describe a procedure used to prepare type-(I + II) QDs with the following structure: CdSe (r = 2.6 nm)/ZnSe (l = 1.7 nm)/CdS (h = 2.2 nm)/ZnS (d = 0.3 nm). We started the synthesis by loading 0.1 mmol $Cd(OA)_2$ and 6 ml ODE into a reaction flask. The mixture was degassed under a vacuum at 110 °C and subsequently filled with nitrogen. After the mixture was heated to 310 °C, 0.2 mmol TOPSe was rapidly injected into the flask, immediately followed by a gradual dropwise addition of 1 ml TOP. This process led to the formation of CdSe cores with r = 1.5 nm. A further increase in the CdSe core radius to 2.6 nm was achieved by the additional injection of $Cd(OA)_2$ (0.25 mmol) and TOPSe (0.25 mmol) precursors.

To grow a compositionally graded $Cd_{1-x}Zn_xSe$ barrier layer on top of the CdSe cores, a solution containing 0.4 mmol $Zn(OA)_2$, 0.19 mmol $Cd(OA)_2$ and 0.38 mmol TOPSe was injected at an elevated temperature (310 °C) and allowed to react with the cores for 30 min. An additional dropwise injection of 1.31 mmol $Zn(OA)_2$ and 1.52 mmol TOPSe was carried out over 30 min, followed by an additional 30 min reaction period to complete the $Cd_{1-x}Zn_xSe$ barrier layer.

To grow a CdS layer, 4 mmol 1-octanethiol was slowly added along with the stepwise injection of $Cd(OA)_2$. For growing an exterior ZnS shell, a mixture containing 2 mmol 1-octanethiol and 4 mmol $Zn(OA)_2$ was injected into the reaction flask. The temperature was then raised to 320 °C and the reaction was allowed to proceed for 1 h. Then, an additional 2 mmol amount of $Zn(OA)_2$ was added, and the reaction continued for 30 min. After the completion of the reaction, the mixture was cooled to room temperature and the synthesized QDs were purified using precipitation/redispersion with acetone/toluene. Subsequently, the purified QDs were diluted with toluene for further use.

Optical characterization

Optical absorption and steady-state PL spectra of the synthesized QDs were measured using a Lambda 950 ultraviolet–visible spectrometer (PerkinElmer) and a FluoroMax+ spectrofluorometer (Horiba), respectively.

Time-resolved PL measurements

Time-resolved PL spectra were measured using a streak camera (Hamamatsu C10910). A continuously stirred QD sample in a 1-mm-thick quartz cuvette was excited by 343 nm (3.6 eV), 190 fs pulses of a tripled output of a regeneratively amplified ytterbium-doped potassium gadolinium tungstate femtosecond laser (PHAROS and HIRO, LIGHT CONVERSION). The pulse repetition rate was 40 kHz. The PL was spectrally dispersed using a Czerny–Turner spectrograph (Acton 2300i) and sent into the streak camera unit to produce a two-dimensional PL intensity map with time as the vertical axis and spectral energy as the horizontal axis. Low-jitter, long-delay data were acquired by triggering the streak unit in a dump mode, where the laser 40 kHz pulse picker signal was used to start the triggering sequence and the first available pulse in the 76 MHz oscillator train was used to generate a stable trigger signal. Using the Hamamatsu slow single-sweep unit, two-dimensional (spectral energy–time) maps were acquired using different time ranges and incident-pump fluences. In the case of the shortest time range used in the experiments (5 ns), the resolution of the streak camera was 12 ps, as inferred from the width of an instrument response function obtained using a femtosecond laser pulse as the input signal.

TA measurements

Purified QDs were loaded into a 1-mm-thick quartz cuvette and stirred continuously. The TA measurements were performed using a pump–probe setup based on a regeneratively amplified ytterbium-doped potassium gadolinium tungstate femtosecond laser (PHAROS, LIGHT CONVERSION) generating 190 fs pulses at 1,030 nm with a 500 Hz repetition rate. Half of the laser fundamental output was used to seed a harmonic generator (HIRO, LIGHT CONVERSION), producing second-harmonic pulses (515 nm or 2.4 eV) used as the pump. The pump beam was modulated using an optical chopper synchronized such that every other pulse was picked from the pulse sequence. The pump pulses were focused into a 120–150-µm-diameter spot onto the sample. The other half of the fundamental laser output at 1,030 nm was fed into an optical delay line with an optical path varied from 0 ns to 4 ns. The delayed pulses were tightly focused onto a 5-mm-thick sapphire plate (EKSMA Optics) to generate a broadband white-light continuum. The generated white light was focused onto the sample into a 90-µm-diameter spot in the middle of the pump spot. The actual pump and probe-beam sizes were measured at the overlap using a beam profiler. The transmitted white light was detected using an Avantes AvaSpec-Fast ULS1350F-USB2 spectrometer.

Pump-induced absorption changes ($\Delta\alpha = \alpha - \alpha_0$) were measured for each pump–probe delay; here α and α_0 are the absorption coefficients of the excited and unexcited samples, respectively. The correction for the probe chirp (spectro-temporal broadening) was performed following the procedure described elsewhere[42]. Excited-state absorption spectra were obtained from $\alpha = \alpha_0 + \Delta\alpha$. The realization of optical gain was indicated by the emergence of spectral regions in which α was negative. Experimentally, this corresponded to the situation when sample excitation led to absorption bleaching ($\Delta\alpha < 0$) and the magnitude of the bleach signal was greater than that of linear absorption: $|\Delta\alpha| > \alpha_0$.

Single-dot measurements

For single-dot studies, QD samples were prepared as dilute sub-single-monolayer films (QD areal density, ~0.01 per µm^2) deposited onto coverslips via drop casting. The samples were excited using 485 nm light generated by a PicoQuant LDH-D-C-485 laser diode. The laser operated at either 250 kHz or 500 kHz repetition rate (100 ps pulse duration) or in the continuous-wave (cw) mode. The excitation beam was focused onto the sample using an Olympus objective lens (×50, 0.70 numerical aperture). The PL signal was collected through the same objective lens. To measure single-dot PL spectra, QD emission

was coupled into an imaging spectrometer (Acton Research, SpectraPro 500i) equipped with a charge-coupled device camera (Princeton Instruments, PYLON). To measure the PL dynamics, QD emission was spectrally filtered and detected by a pair of avalanche photodiodes (Micro Photon Devices, PDM Series) coupled to a start–stop time correlator (PicoQuant, HydraHarp 400). The temporal resolution of these measurements was 300 ps.

To isolate biexciton decay from single-exciton dynamics, we applied two-photon correlation measurements conducted using the Hanbury Brown–Twiss (HBT) setup[43]. In this experiment, the emission from an individual QD is split between two channels equipped with single-photon detectors. Correlations between photon arrival events as a function of the time difference between the two channels (τ) yield information about second-order intensity correlation function $g^{(2)}(\tau)$. In the case of pulsed measurements, a non-zero $g^{(2)}$ signal at $\tau = 0$ implies that one pump pulse produced two photons, that is, the emitting state was a biexciton. Hence, the statistics of the delay of the first detected photon versus the pump pulse can be used to reconstruct biexciton dynamics.

The HBT setup was also used to evaluate the biexciton emission quantum yields q_{XX}. The HBT determination of q_{XX} uses the fact that the ratio of the $g^{(2)}$ amplitudes for the central ($\tau = 0$) and side ($\tau = T$) peaks is determined by the ratio of the biexciton and single-exciton PL quantum yields[44,45] (T is the interpulse separation in a pump–pulse sequence).

All the measurements were performed at room temperature under ambient conditions. The analysis of the experimental data was performed using custom-built software developed in Python (v3.9).

Liquid-state QD laser

A solution sample of QDs in toluene with a concentration of about 14 μmol l^{-1} was loaded into a 1-cm-wide, 1-mm-thick quartz cuvette. The cuvette was placed inside a cavity composed of a high-reflectivity mirror and a reflection grating having 2,400 grooves mm^{-1} (Thorlabs). The wide side of the cuvette was aligned with the cavity axis. The grating angle was selected to send the first-order ($m = 1$) diffraction beam back into the cavity (Littrow configuration). The zeroth-order ($m = 0$) diffraction was used to outcouple light from the cavity. The cavity resonance was tuned by rotating the grating assembly, which allowed us to tune the output wavelength. Two intracavity lenses were used to collimate the beam and to ensure uniform illumination on the grating. The QD sample was excited from a wider side of the cuvette using 532 nm, 5 ns second-harmonic pulses of a Nd:YAG laser (Amplitude Laser, Minilite II). The pump beam was shaped as a 1-cm-long, 200-μm-wide horizontal stripe using two cylindrical lenses.

The spectral analysis of the output beam of liquid-state QD lasers was performed using an imaging spectrometer (Acton Research, SpectraPro 500i) paired with a charge-coupled device camera (Princeton Instruments, PYLON). The spectral resolution of this system was 120 μeV.

Measurements of temporal coherence

We used a Michelson interferometer to measure the temporal coherence of the QD laser output. In these measurements, the beam was split between two channels using a non-polarizing 50/50 beamsplitter. Each channel was equipped with a flat mirror reflecting light back towards the beamsplitter. One of the mirrors was mounted onto a single-axis linear delay stage (Aerotech ANT130L), which allowed us to control the time delay between the two paths. After passing the beamsplitter, the two interfering beams were directed along the same path where they were collected using an Olympus PLN ×10 objective used to couple light into a single-photon avalanche photodiode (Micro Photon Devices, PDM series). To record the intensity of the interference pattern, we used a time-tagged, time-resolved mode provided by a time-correlated single-photon-counting module (PicoQuant HydraHarp 400). The subsequent analysis of the time-tagged, time-resolved data was performed using a Python code.

Measurements of divergence

Beam divergence was assessed by measuring the beam radius (R_{beam}) with a beam profiler (BladeCam-HR, DataRay). The light intensity profile was recorded as a function of distance from the cavity (z), and the beam halfwidth at the $1/e^2$ intensity level was used as a measure of beam radius. The collected data were fitted to a hyperbolic function $R_{beam} = w_0(1 + z\tan(\theta))^{0.5}$, where θ is the divergence half-angle and w_0 is the beam-waist radius.

Reporting summary

Further information on research design is available in the Nature Portfolio Reporting Summary linked to this article.

Data availability

Source data are provided with this paper. The remaining data are available from the corresponding author upon reasonable request.

References

42. Livache, C. et al. High-efficiency photoemission from magnetically doped quantum dots driven by multi-step spin-exchange Auger ionization. *Nat. Photon.* **16**, 433–440 (2022).
43. Brown, R. H. & Twiss, R. Q. Correlation between photons in two coherent beams of light. *Nature* **177**, 27–29 (1956).
44. Nair, G., Zhao, J. & Bawendi, M. G. Biexciton quantum yield of single semiconductor nanocrystals from photon statistics. *Nano Lett.* **11**, 1136–1140 (2011).
45. Park, Y. S. et al. Near-unity quantum yields of biexciton emission from CdSe/CdS nanocrystals measured using single-particle spectroscopy. *Phys. Rev. Lett.* **106**, 187401 (2011).
46. Park, Y.-S., Bae, W. K., Padilha, L. A., Pietryga, J. M. & Klimov, V. I. Effect of the core/shell interface on Auger recombination evaluated by single-quantum-dot spectroscopy. *Nano Lett.* **14**, 396–402 (2014).

Acknowledgements

This project was supported by the Laboratory Directed Research and Development (LDRD) program at the Los Alamos National Laboratory under project no. 20230352ER. V.P. and N.A. acknowledge support from a LANL Director's Postdoctoral Fellowship. We thank P. R. Bowlan and P. J. Skrodzki for providing access to the Nd:YAG laser used as a pump source in the QD liquid-state lasing experiments.

Author contributions

V.I.K. initiated the study and, together with D.H., conceived the idea of 'hybrid biexciton' optical gain. V.I.K. also analysed the data and coordinated the project execution. D.H. and J.N. synthesized the type-(I+II) QDs and performed their structural analysis. C.L. and V.P. carried out the TA and time-resolved PL measurements. D.H. performed the single-dot spectroscopic measurements of the type-(I+II) QDs and also conducted the quantum-mechanical calculations of their electronic structures. X.L., J.D. and K.W. performed the initial optical gain and ASE studies of liquid QD suspensions using the cg-QD samples. V.P., D.H., C.L. and N.A. developed the laser cavity design and performed the liquid-state lasing experiments with type-(I+II) QDs. D.H. and V.I.K. wrote the manuscript with inputs from all co-authors.

Competing interests

The authors declare no competing interests.

Additional information

Extended data is available for this paper at https://doi.org/10.1038/s41563-024-02048-y.

Supplementary information The online version contains supplementary material available at https://doi.org/10.1038/s41563-024-02048-y.

Correspondence and requests for materials should be addressed to Victor I. Klimov.

Peer review information *Nature Materials* thanks Uri Banin and the other, anonymous, reviewer(s) for their contribution to the peer review of this work.

https://doi.org/10.1038/s41563-024-02048-y

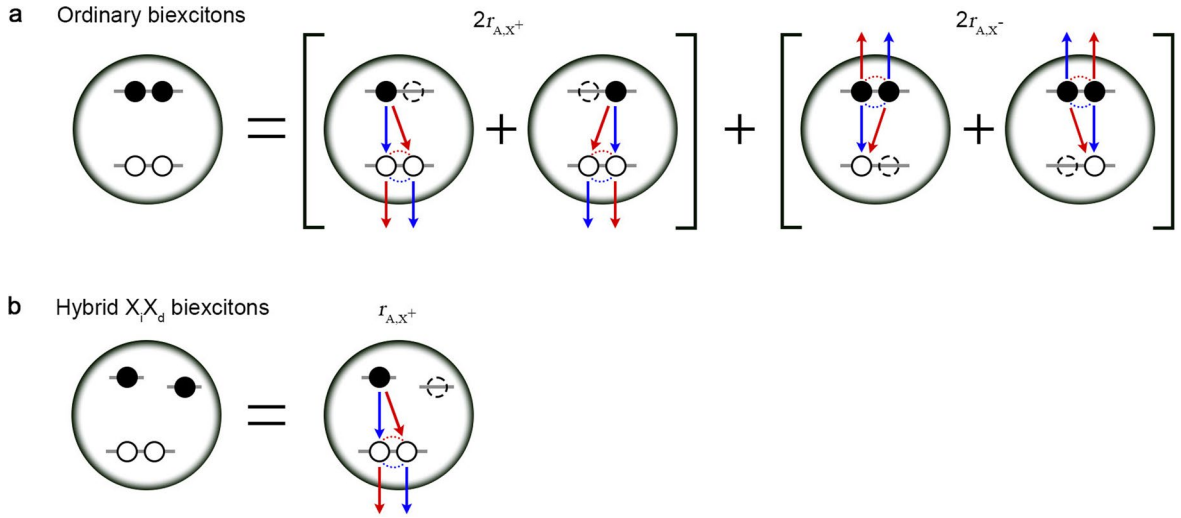

Extended Data Fig. 1 | Application of the superposition principle to Auger decay of an ordinary (XX) biexciton and a hybrid (X_iX_d) biexciton. a, According to the superposition principle, the Auger decay rate of any multicarrier state can be presented as the sum of the rates of independent negative and positive trion Auger pathways (r_{A,X^-} and r_{A,X^+}, respectively)[24,29,46]. In the case of an ordinary biexciton, there are 2 negative trion pathways and 2 positive trion pathways. Therefore, the overall Auger rate is $r_{A,XX} = 2r_{A,X^-} + 2r_{A,X^+}$. **b**, In the case of a hybrid X_iX_d biexciton, the pathways involving the indirect transition can be neglected, leaving only one positive-trion pathway active. This yields $r_{A,XiXd} = r_{A,X^+}$.

https://doi.org/10.1038/s41563-024-02048-y

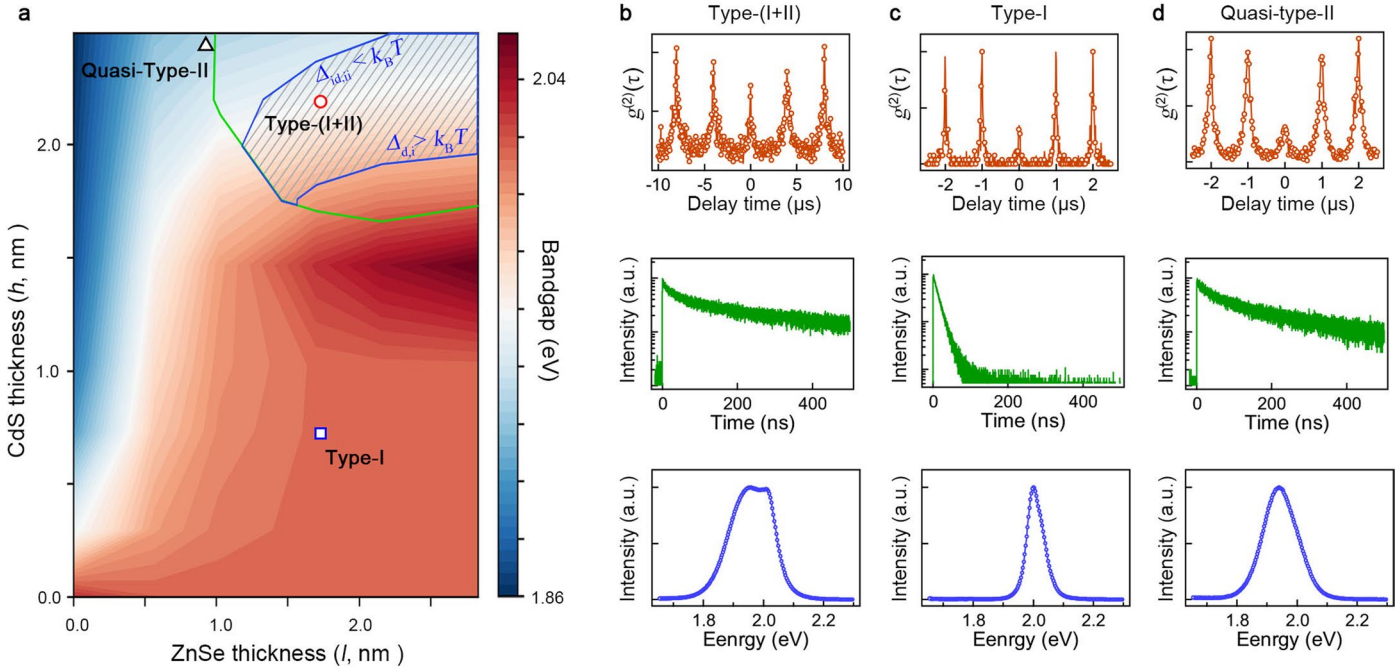

Extended Data Fig. 2 | Modeling of electronic states and measurements of CdSe/ZnSe/CdS/ZnS QDs. a, Calculated band-edge transition energy of the CdSe (r = 2.6 nm)/ZnSe (l)/CdS (h)/ZnS (d = 0.3 nm) QDs as a function of l and h. The region within the green boundary corresponds to the regime of well-defined indirect and direct exciton states, as indicated by the electron-hole (e-h) overlap integrals (θ_{eh}) of <0.1 and >0.9 for the lowest and the first excited e-h states, respectively. The region within the blue boundary corresponds to the regime where we simultaneously satisfy the conditions $\Delta_{d,i} = E_d - E_i > k_BT$ and $\Delta_{id,ii} = E_{id} - E_{ii} < k_BT$ (k_B is the Boltzmann constant and T is the temperature; it is assumed that T is 300 K). According to our simulations (Supplementary Note 1), this automatically implies that we also satisfy the condition $\Delta_{dd,id} = E_{dd} - E_{id} > k_BT$. Thus, the region highlighted by the diagonal grey lines corresponds to the QD dimensions for which all requirements necessary for the realization of hybrid direct/indirect biexcitons are satisfied. **b-d**, Single-dot and ensemble measurements of three CdSe/ZnSe/CdS/ZnS QD samples, the dimensions of which correspond to three different points in the diagram shown in panel **a**: **(b)** red open circle (l = 1.7 nm, h = 2.2 nm; same sample as in Figs. 2 to 4); **(c)** blue open square (l = 1.7 nm, h = 0.7 nm); **(d)** black open triangle (l = 0.9 nm, h = 2.4 nm). The top row shows single-dot second-order intensity correlation ($g^{(2)}$) measurements. The middle row presents the spectrally integrated ensemble PL dynamics measured using low-intensity (sub-single-exciton) pulsed excitation with a photon energy of 2.54 eV. The bottom presents the ensemble PL spectra of the QDs obtained using low-intensity *cw* excitation with a photon energy of 2.76 eV. The observed characteristics of the samples shown in panels **c** and **d** are consistent with those of type-I and quasi-type-II QDs[31,33], respectively.

https://doi.org/10.1038/s41563-024-02048-y

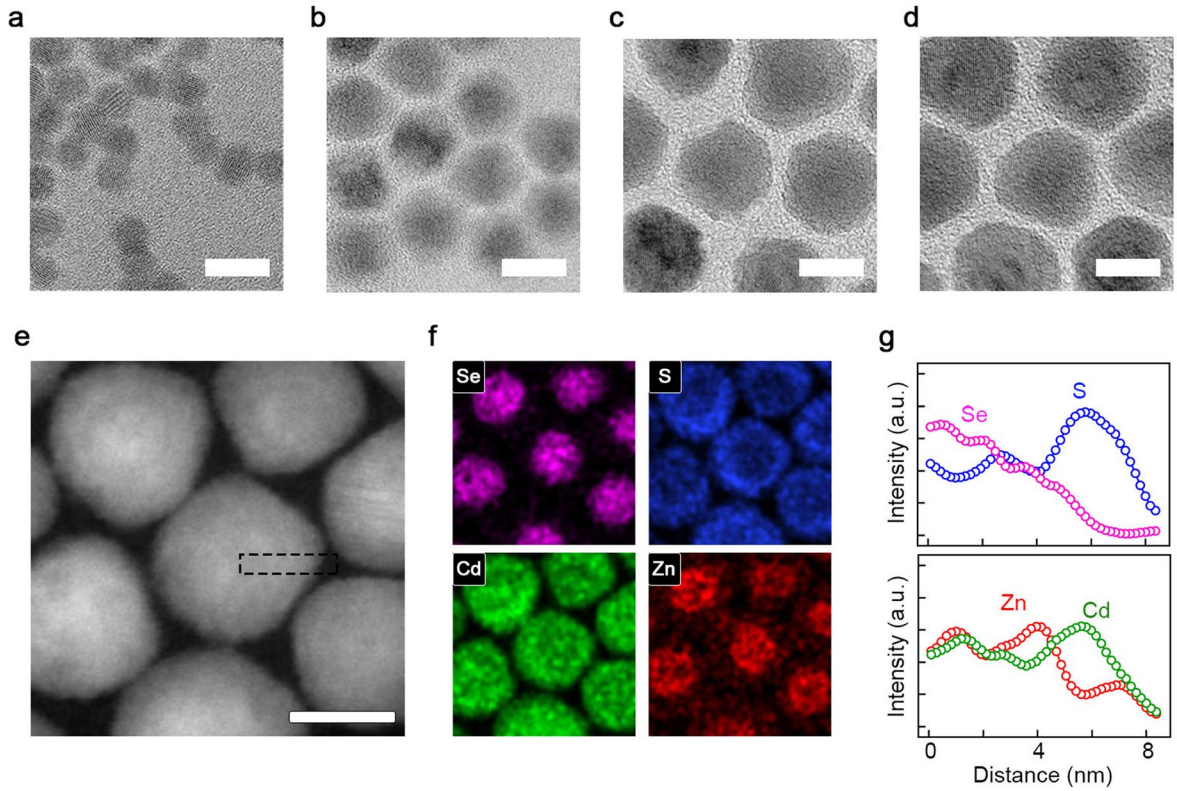

Extended Data Fig. 3 | Structural characteristics of final type-(I+II) QDs and intermediate structures. a-d, Transmission electron microscope (TEM) images illustrating the progression of the synthesis of the type-(I+II) CdSe (r = 2.6 nm)/ZnSe (l = 1.7 nm)/CdS (h = 2.2 nm)/ZnS (d = 0.3 nm) QDs: (**a**) CdSe cores, (**b**) CdSe/ZnSe QDs, (**c**) CdSe/ZnSe/CdS QDs, and (**d**) final CdSe/ZnSe/CdS/ZnS QDs. **e**, Scanning transmission electron microscope (STEM) image of type-(I+II) QDs. Scale bar is 10 nm. **f**, Energy-dispersive X-ray spectroscopy (EDS) elemental maps for Se (magenta), S (blue), Cd (green), and Zn (red). **g**, Elemental radial profiles extracted from EDS maps for the region shown in panel **e** by the dashed box.

https://doi.org/10.1038/s41563-024-02048-y

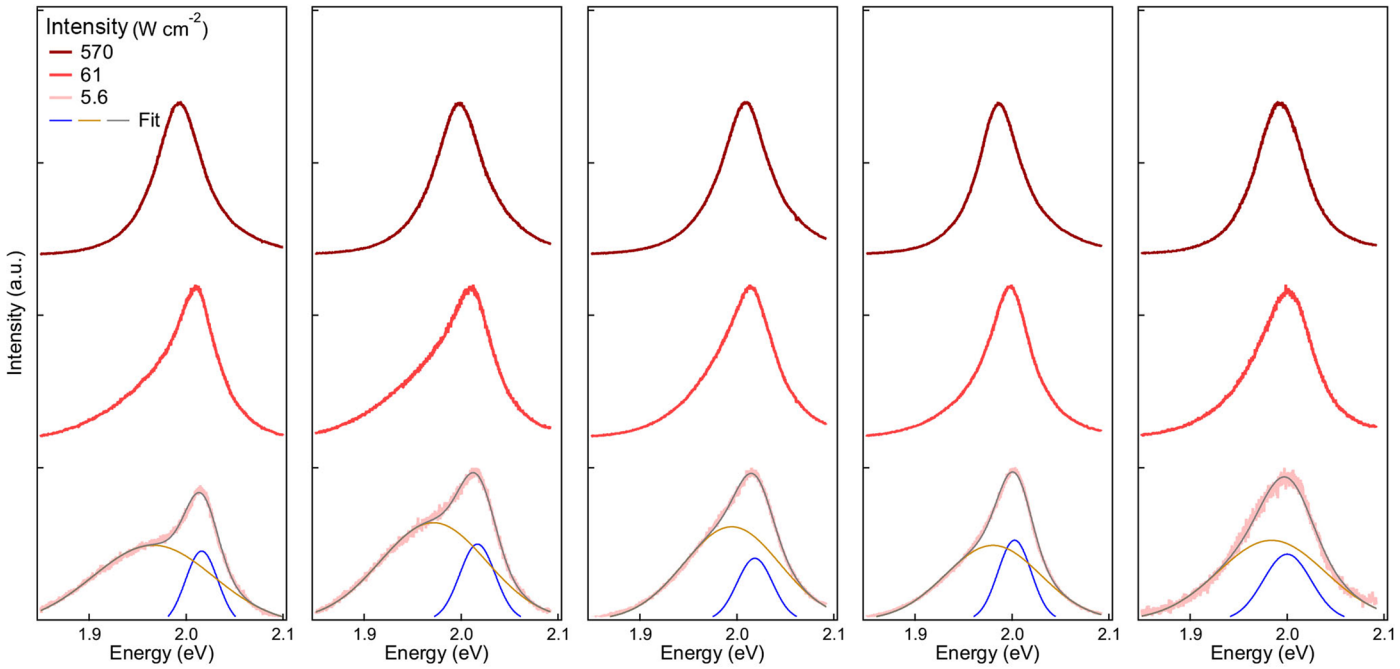

Extended Data Fig. 4 | PL spectra of individual type-(I+II) QDs at different pump intensities. Representative measurements of single-dot PL spectra for 5 individual type-(I+II) QDs conducted using *cw* excitation with a photon energy of 2.54 eV and an intensity of 5.6, 61 and 570 W cm^{-2}. The PL spectrum with the lowest pump intensity is presented as a sum of two Gaussian bands describing the emission spectra of direct and indirect excitons (narrower and wider bands, respectively).

https://doi.org/10.1038/s41563-024-02048-y

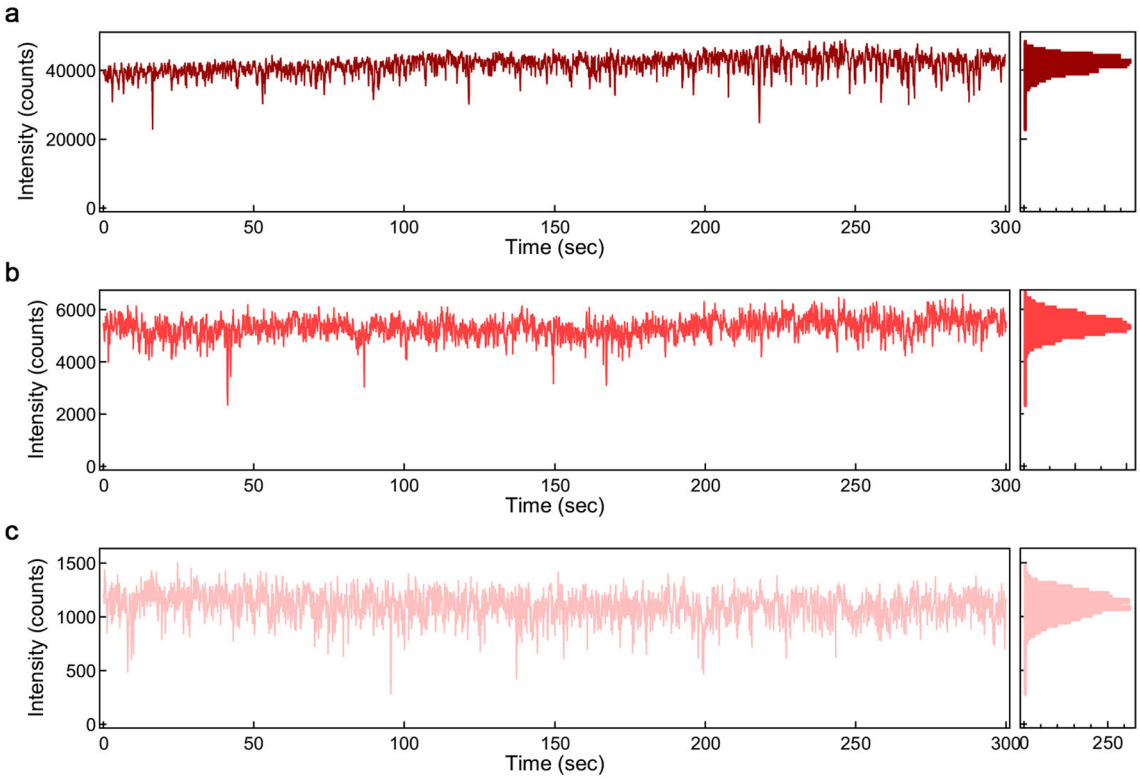

Extended Data Fig. 5 | Single-dot PL intensity trajectories of type-(I+II) QDs. a-c, Single-dot PL trajectories (left panels) and corresponding histograms (right panels) measured for an individual type-(I+II) QD using *cw* excitation with a photon energy of 2.54 eV and different pump intensities: (**a**) 570 W cm^{-2}, (**b**) 61 W cm^{-2}, and (**c**) 5.6 W cm^{-2}.

https://doi.org/10.1038/s41563-024-02048-y

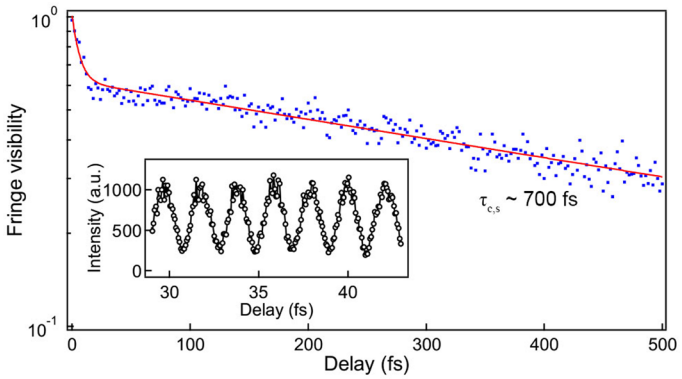

Extended Data Fig. 6 | Measurements of temporal coherence of a laser beam using Michelson interferometry. The fringe visibility as a function of the time delay between the two interferometer arms (blue points) is fitted to the biexponential decay (red line). The time constant of the longer-lived component is ~700 fs. The inset shows a representative interferogram.

https://doi.org/10.1038/s41563-024-02048-y

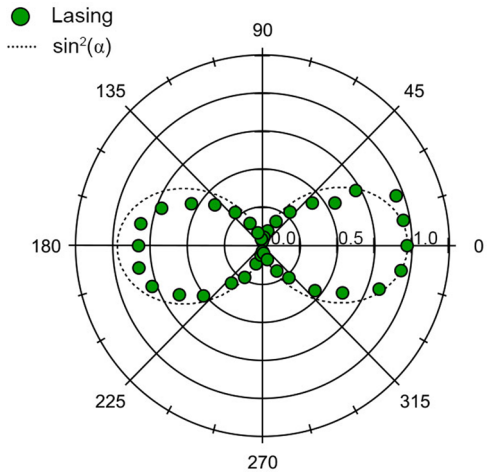

Extended Data Fig. 7 | Polarization measurements of a laser beam. The emission intensity collected through a linear polarizer as a function of the polarizer angle (green circles) shown using polar coordinates. The dotted line represents the ideal $\sin^2(\alpha)$ dependence expected for a perfectly linearly polarized beam. These measurements indicate a high degree of linear polarization of 0.95.

https://doi.org/10.1038/s41563-024-02048-y

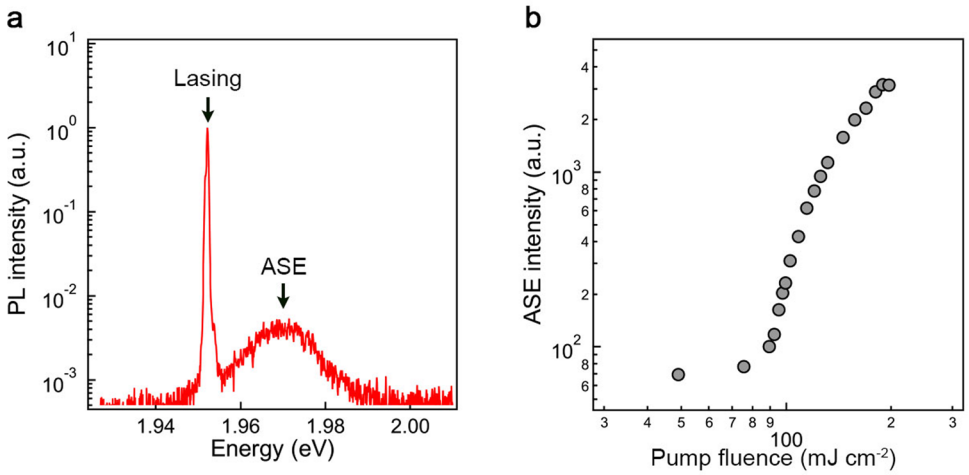

Extended Data Fig. 8 | Lasing versus ASE. a, Representative spectrum of a liquid laser based on type-(I+II) CdSe QDs with $r = 2.6$ nm, $l = 1.7$ nm, $h = 2.2$ nm, and $d = 0.3$ nm. The narrow line at 1.952 eV is due to lasing, and the broader band at 1.97 eV is due to ASE. The amplitude of the ASE band is more than two orders of magnitude smaller than the amplitude of the lasing line (the vertical axis is logarithmic). The QD gain medium is excited using second harmonic pulses of a Nd:YAG laser (photon energy 2.33 eV, pulse duration 5 ns, repetition rate 10 Hz). **b**, The ASE signal intensity as a function of pump level indicates an ASE threshold of 89 mJ cm^{-2}. This is approximately twice the lasing threshold.

https://doi.org/10.1038/s41563-024-02048-y

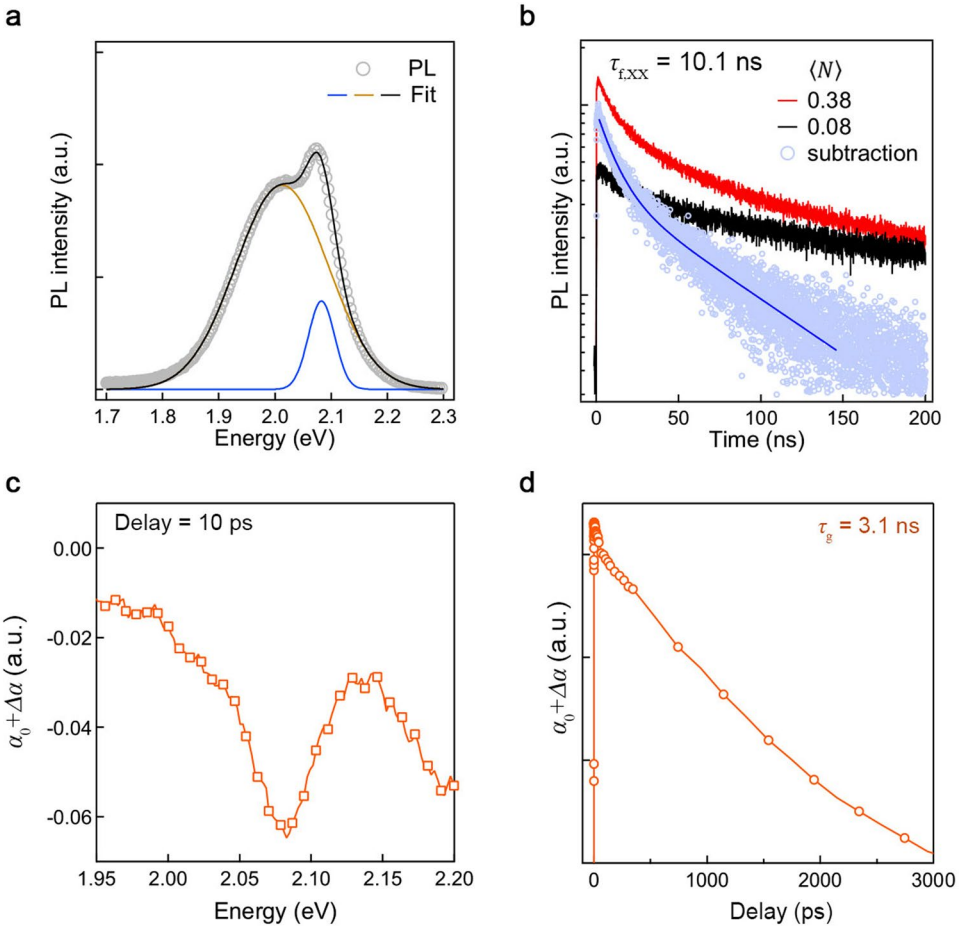

Extended Data Fig. 9 | PL and optical gain characteristics of wider-bandgap type-(I+II) QDs. a, PL spectrum of type-(I+II) CdSe QDs with $r = 2.3$ nm, $l = 2.2$ nm, $h = 1.6$ nm, and $d = 0.3$ nm. The experimental data are shown as open grey circles, and the double Gaussian fit is shown as a black line. The two individual Gaussian bands used in the fit are shown as blue and orange lines. The PL spectrum was measured using *cw* excitation with a photon energy of 2.76 eV. **b**, PL dynamics of the same sample collected for two different pump levels: $\langle N \rangle = 0.08$ (black) and 0.38 (red) (the traces are normalized to match the signal intensity at 500 ns). The biexciton dynamics obtained by subtracting these two traces are shown as blue circles. A biexponential fit (blue line) yields a hybrid (direct/indirect) biexciton lifetime of 10.1 ns. The sample was excited using 190 fs, 3.1 eV pulses. **c**, The TA spectrum of wider bandgap type-(I+II) QDs presented as the excited state absorption coefficient (α) for a pump-probe delay of 10 ps and an excitation level $\langle N \rangle = 54$ (190 fs, 2.4 eV pump pulses). The optical gain regime corresponds to $\alpha < 0$. **d**, The TA dynamics yields an optical gain lifetime of 3.1 ns.

https://doi.org/10.1038/s41563-024-02048-y

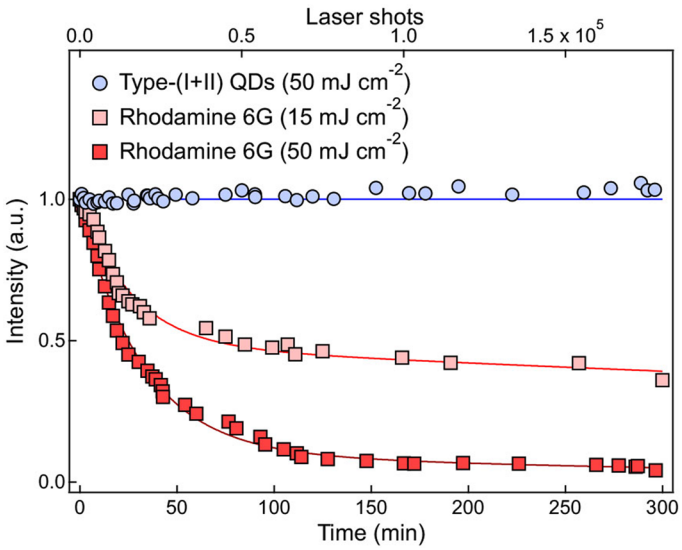

Extended Data Fig. 10 | Comparison of operational stability of lasers based on type-(I+II) QDs and rhodamine 6G dye. Comparison of laser output intensity as a function of time for a solution of type-(I+II) QDs (r = 2.6 nm, l = 1.7 nm, h = 2.2 nm, and d = 0.3 nm) (blue circles) and rhodamine 6G dye (pale red and red squares). In both cases, the gain medium was excited by 532 nm, 5 ns, 10 Hz second harmonic pulses of a Nd:YAG laser. The QDs were dispersed in toluene, and rhodamine 6G was dissolved in a mixture of methanol and ethylene glycol (5:95 %, v/v). During the measurements, both solutions were in 'static form', that is, they were not stirred, flowed or otherwise agitated. During the stability test, the type-(I+II) QDs were excited using a per-pulse fluence of approximately 50 mJ cm^{-2}. The rhodamine 6G dye was excited using a per-pulse fluence of 15 mJ cm^{-2} (pale red) and 50 mJ cm^{-2} (red); the former intensity corresponded to excitation near the lasing threshold (14 mJ cm^{-2}). The dye laser output intensity decreased continuously during the test. The initial rapid decay could be fitted to an exponential relaxation with a time constant of 30 min.

nature research

Corresponding author(s): Victor I. Klimov

Lasing Reporting Summary

Nature Research wishes to improve the reproducibility of the work that we publish. This form is intended for publication with all accepted papers reporting claims of lasing and provides structure for consistency and transparency in reporting. Some list items might not apply to an individual manuscript, but all fields must be completed for clarity.

For further information on Nature Research policies, including our data availability policy, see Authors & Referees.

Experimental design

Please check: are the following details reported in the manuscript?

1. Threshold

Plots of device output power versus pump power over a wide range of values indicating a clear threshold	☒ Yes ☐ No	Fig. 5b is the plot of the output beam intensity as a function of pump fluence. It shows a clear lasing threshold of 44 mJ/cm^2. There is virtually no output signal before the threshold.
		Explain why this information is not reported/not relevant.

2. Linewidth narrowing

Plots of spectral power density for the emission at pump powers below, around, and above the lasing threshold, indicating a clear linewidth narrowing at threshold	☒ Yes ☐ No	Fig. 2b shows the emission spectrum of a cavity-free sample measured under low-intensity (sub-single-exciton) excitation. The linewidth of this spectrum is ~160 meV. In the lasing regime, the same sample shows narrow-band emission with the linewidth of 0.38 meV (inset of Fig 5e).
		Explain why this information is not reported/not relevant.
Resolution of the spectrometer used to make spectral measurements	☒ Yes ☐ No	The spectral resolution used in the lasing studies was 0.12 meV (see Methods).
		Explain why this information is not reported/not relevant.

3. Coherent emission

Measurements of the coherence and/or polarization of the emission	☒ Yes ☐ No	Both temporal coherence and polarization measurements were conducted (Extended Data Figs. 6 and 7, respectively).
		Explain why this information is not reported/not relevant.

4. Beam spatial profile

Image and/or measurement of the spatial shape and profile of the emission, showing a well-defined beam above threshold	☒ Yes ☐ No	The intensity beam profile measurements are presented in Fig. 5c. The measurements of beam divergence are displayed in Fig. 5d.
		Explain why this information is not reported/not relevant.

5. Operating conditions

Description of the laser and pumping conditions *Continuous-wave, pulsed, temperature of operation*	☒ Yes ☐ No	A detailed description of operating conditions is included in the main text. It is also available in Methods and figure captions.
		Explain why this information is not reported/not relevant.
Threshold values provided as density values (e.g. W cm^{-2} or J cm^{-2}) taking into account the area of the device	☒ Yes ☐ No	Yes, the lasing threshold is presented in terms of J/cm^2 (Fig. 5b).
		Explain why this information is not reported/not relevant.

6. Alternative explanations

Reasoning as to why alternative explanations have been ruled out as responsible for the emission characteristics *e.g. amplified spontaneous, directional scattering; modification of fluorescence spectrum by the cavity*	☒ Yes ☐ No	We discuss a potential influence of ASE and provide evidence that the observed narrow-band, highly direction emission is not due to ASE but due to laser oscillations (main text and Extended Data Fig. 8).
		Explain why this information is not reported/not relevant.

7. Theoretical analysis

Theoretical analysis that ensures that the experimental values measured are realistic and reasonable *e.g. laser threshold, linewidth, cavity gain-loss, efficiency*	☒ Yes ☐ No	We conduct a theoretical analysis of a critical QD density needed for lasing. The calculated values are in good agreement with the actual QD densities leading to the lasing effect.
		Explain why this information is not reported/not relevant.

8. Statistics

Number of devices fabricated and tested	☒ Yes ☐ No	We have tested two differently sized samples of the type-(I+II) QDs (captions of Figs. 5b and 5e). The QD samples with the dimensions described in Fig. 2 were prepared via 4 separate reactions. So, we have studied 5 QD batches total. The solution samples from all 5 batches have shown the lasing effect. We have also tested several different QD concentrations. All concentrations from 14–30 µmol/L produced stable lasing. In addition, we have tested two different cavities, one with a beam expander and one without it. Both have shown lasing. Due to improved spectral selectivity, the cavity with the beam expander shows a narrower emission line (0.38 meV) than the cavity without the expander (2 meV). *Explain why this information is not reported/not relevant.*
Statistical analysis of the device performance and lifetime (time to failure)	☒ Yes ☐ No	Extended Data Fig. 10 displays studies of the operational stability of the QD laser vs. the dye laser. *Explain why this information is not reported/not relevant.*